energies

MDPI

Article

Integrated Vehicle-Following Control for Four-Wheel Independent Drive Based on Regenerative Braking System Control Mechanism for Battery Electric Vehicle Conversion Driven by PMSM 30 kW

Pataphiphat Techalimsakul [1] and Wiwat Keyoonwong [2,*]

[1] Program in Electronics and Automation Systems Engineering, Faculty of Technical Education, Rajamangala University of Technology Thanyaburi, Khlong Hok 12110, Thailand; pataphiphat_t@rmutt.ac.th
[2] School of Engineering, King Mongkut's Institute of Technology Ladkrabang, Bangkok 10520, Thailand
* Correspondence: wiwat.ke@kmitl.ac.th; Tel.: +66-2329-8000

Abstract: This study proposed the hybrid energy storage paradigm (HESP) equipped with front-wheel permanent magnet synchronous motors (PMSMs) for battery electric vehicles (BEVs). In this case, all four wheels are driven by a single motor using mechanical coupling to distribute the motor's power to each wheel evenly. The HESP is a combination of several supercapacitors (SCs) and an NMC-lithium battery equipped with an advanced artificial neural network (ANN) that will enhance the regenerative braking system (RBS) efficiency of energy storage during braking. The three-phase inverter switching algorithm ensures efficient regenerative braking and fine adjustment of the brake force distribution. Under the RBS, the HESP with the ANN first transfers braking energy to the SC and, when the safety standard is reached, the SC transfers it to the battery. The RBS control maintains an even distribution of braking force at all distances to ensure stability during braking. The results show that a traditional BEV can drive 245.46 km (35 cycles), while an EV with an RBS-only battery can drive 282.56 km (40 cycles). An EV with HESP-RBS can drive 338.78 km (48 cycles), which is an increase of 93.32 km (13 cycles). The HESP-RBS increased the regenerative efficiency by 38.01% when compared to a traditional BEV.

Keywords: electric vehicles; regenerative braking; supercapacitors; conversion; PMSM

check for updates

Citation: Techalimsakul, P.; Keyoonwong, W. Integrated Vehicle-Following Control for Four-Wheel Independent Drive Based on Regenerative Braking System Control Mechanism for Battery Electric Vehicle Conversion Driven by PMSM 30 kW. *Energies* **2024**, *17*, 2576. https://doi.org/10.3390/en17112576

Academic Editor: Frede Blaabjerg

Received: 14 March 2024
Revised: 16 May 2024
Accepted: 21 May 2024
Published: 26 May 2024

Copyright: © 2024 by the authors. Licensee MDPI, Basel, Switzerland. This article is an open access article distributed under the terms and conditions of the Creative Commons Attribution (CC BY) license (https://creativecommons.org/licenses/by/4.0/).

1. Introduction

Presently, a mounting concern surrounds air pollution, propelled by the ongoing trend of economic growth and the increase in private car ownership. The emission of greenhouse gases from combustion engine vehicles has compounded these environmental concerns. In this context, battery electric vehicles (BEVs) are assuming a more significant role, driven by advancements in battery technology and the pressing demand for sustainable transportation solutions. Significantly, the allure of electric trains resides in their quiet operation and absence of emissions, both of which are advantageous for the environment [1–5].

Among growing concerns about environmental pollution and the energy crisis, electric vehicles have become a focus for research and development in countries across the globe [6]. However, most battery electric vehicles operate using electrochemical batteries as their primary energy storage system. Electrochemical batteries come with several disadvantages including short lifespan, restricted driving range, low power density, and high cost, which reduce the effectiveness of regenerative braking [7].

To resolve various limitations, a hybrid energy storage paradigm for a regenerative braking system (HESP-RBS) employing a combination of batteries and supercapacitors (SCs) was adopted, aiming to enhance vehicle acceleration and extend battery lifespan. Moreover, other HESP alternatives have been introduced for BEVs. Specifically, the proposed HESP

focuses on the advantages of the high energy density of SCs and batteries. However, the high-power electronic interface of a bidirectional DC/DC chopper contributes to cost inefficiency and, in addition, there is fast battery degradation [8,9].

With enhanced SC innovation, the SC integrates the high potential energy density characteristics of an electrochemical double-layer capacitor (EDLC) with its pseudocapacitor with high energy density characteristics. A comparison of SC and NMC-lithium battery properties is shown in Table 1. The HESP model combining SC and NMC-lithium batteries has the potential to achieve both the outstanding exceptional power density of the SC and the critical energy density of the battery. Therefore, in this paper, the recommended HESP setup consists of a multiple-cell battery unit, SC module, and high-power unidirectional DC/DC chopper. This scaleup transitioned from laboratory testing to industrial-scale implementation, employing high-grade batteries and permanent magnet synchronous motors (PMSMs) for real road electric vehicles. PMSMs are well-suited for regenerative braking systems, allowing them to efficiently convert kinetic energy into electrical energy during braking or deceleration. Furthermore, opting for unidirectional charging over bidirectional charging is anticipated to yield cost savings and promote battery longevity [10]. Further, this research proposes the use of a single motor with a mechanical coupling system for all four wheels to achieve four-wheel drive capability while maintaining efficiency and reliability. The single motor's torque is distributed to all four wheels through differentials and a driveshaft system.

Table 1. The different characteristics of the supercapacitor and NMC-lithium battery [8,9].

Key Characteristic	Supercapacitor (SC)	NMC-Lithium Battery
Cell voltage	2.1–3.3 V	3.6–4.2 V
Specific energy	5 Wh/kg	100–200 Wh/kg
Specific power	10 kW/kg	1–3 kW/kg
Cost per Wh	>USD 10	USD 0.50–1
Service life	10+ years	5–10 years
Time (charge)	5–15 s	10–90 min
Time (discharge)	Sec/Minutes	Minutes/Hours
Efficiencies	>95%	80–96%
Number of cycles	Millions of times	500 times

This study conducts experiments on the HESP framework of a recommended SC/NMC-lithium battery of a four-wheel BEV powered by a three-phase PMSM. The investigation spans four distinct operational scenarios: the normal scenario, the acceleration scenario, and the SC and battery activated regenerative braking scenario as shows how of the working system in Figure 1. To increase vehicle performance, an ANN-equipped control mechanism for the RBS has been implemented, a mechanism that aims to increase vehicle acceleration and extend life. The study structure is as follows: Section 1 is an introduction; Section 2 offers an in-depth exploration of the HESP, focusing on its various functional scenarios and configurations; Section 3 elaborates on the innovative control mechanism equipped with the ANN that drives the proposed RBS; Section 4 presents the outcomes derived from simulations and real-world experiments conducted on the suggested regenerative braking scenario; and Section 5 provides the conclusion.

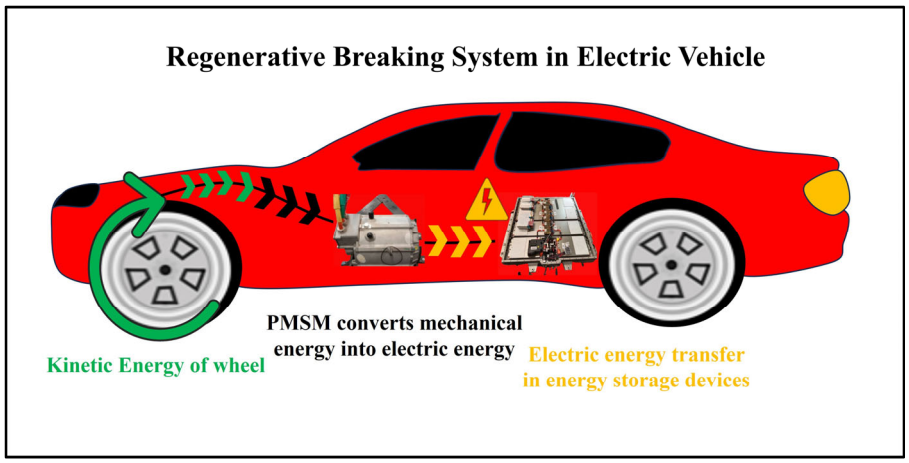

Figure 1. How the new RBS of an electric vehicle works.

2. The HESP and Functional Scenario

Figure 2 shows the experimental hybrid energy storage paradigm (HESP), which comprises three main components: the SC unit with multiple cells, the battery unit featuring multiple cells, and a unidirectional DC/DC chopper. Direct DC link connection to the battery ensures stability and linking the battery to the SC unit involves the use of a unidirectional DC/DC chopper. This arrangement guarantees that the voltage of the SC unit remains higher than that of the battery. Additionally, a regenerative diode (D_3) is used to connect the SC unit in parallel with the battery. The voltage generated by the HESP is then supplied to the three-phase inverter, which, in turn, powers a three-phase PMSM. The HESP operates in four distinct scenarios: the normal scenario, the acceleration scenario, and the SC and NMC-lithium battery activated regenerative braking scenario [10].

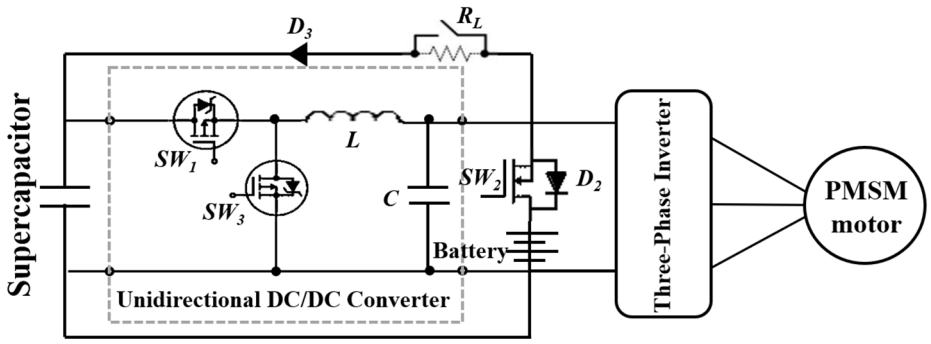

Figure 2. The schematic proposed HESP structure.

In the normal scenario, the battery's power output adequately fulfills the vehicle power requirements, resulting in the SC voltage being higher compared to the battery voltage. Consequently, the reverse conducting power diode of D_3 comes into play. In this scenario, the battery functions as the exclusive voltage source for the three-phase PMSM. Figure 3 shows a diagram of the HESP system during a normal functional scenario [10].

In the acceleration scenario, the power of the motor P_{motor} will be greater battery power rating $P_{Batt,rated}$. The battery enters deep discharge cycles, which impairs the vehicle's drivability. Therefore, the SC will maintain a level to boost the battery until the SC voltage is greater than the battery voltage. In this condition, D_2 will always be in a reverse conducting state, and energy from both SC and the battery will be used to power the PMSM. The SC of the HESP system can rapidly discharge to supplement battery power. This is especially true in such situations due to the high energy demand. Figure 4 provides an illustrative representation of the energy flow during acceleration conditions [10].

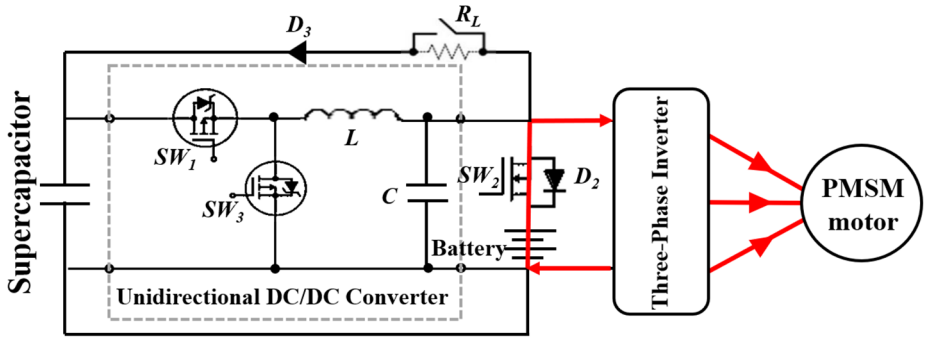

Figure 3. The energy transference within the HESP under the normal scenario.

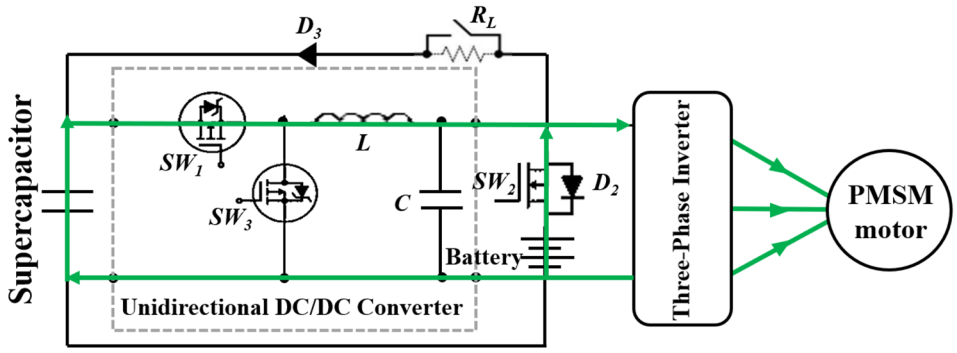

Figure 4. The energy transference within the HESP under the acceleration scenario.

During deceleration, the regenerative braking system activates, converts kinetic energy into electrical energy, and stores it in the SC or battery. The performance of HESP-RBS during deceleration directly affects its ability to recover and store energy efficiently.

In the SC regenerative braking scenario, the pressure of the DC link needs to be in a boost state, so D_2 is forward conducting, and braking energy can be transferred and stored to the SC (Figure 5). Traditionally, an additional buck–boost DC chopper transfers the braking energy to the SC. However, this approach is burdened with heightened implementation expenses and reduced energy transfer efficiency resulting from power dissipation. To overcome this, the integration of inductors into a three-phase PMSM can be considered, alongside the optimal switching scheme generated by an ANN through the bidirectional three-phase inverter [10].

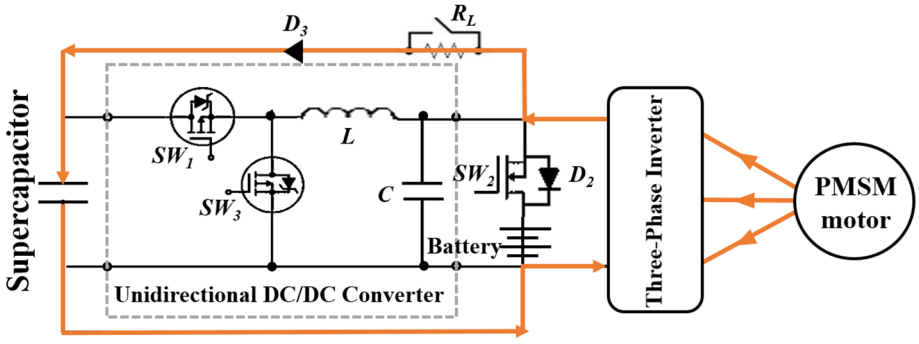

Figure 5. The energy transference within the HESP under the SC activates a regenerative braking scenario.

In the NMC-lithium battery regenerative braking scenario, if the SC voltage is less than or equal to the SC maximum standard voltage ($V_{SC} \geq V_{SC,max}$), braking energy cannot be transferred to the SC anymore. For this reason, regeneration during braking is switched to the battery [10]. The principle of operation in this scenario resembles the previous scenario,

the DC link voltage can be increased, and then energy from braking is transferred to the battery via D_2, as shown in Figure 6.

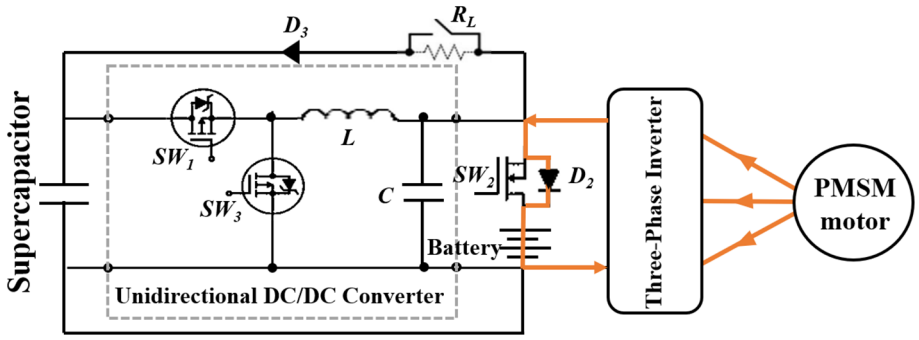

Figure 6. The energy transference within the HESP under the NMC-lithium battery activates a regenerative braking scenario.

3. Presentation of Regenerative Braking System

Equivalent circuits of the proposed inverter, PMSM, and HESP are shown in Figure 7, where EMF_a, EMF_b, and EMF_c are the back-EMF shields of the a, b, and c phases, respectively. During the regenerative braking scenario, the DC link voltage undergoes amplification, leading to the accumulation of braking energy in the SC through D_3, followed by transfer to the battery through D_2 [11].

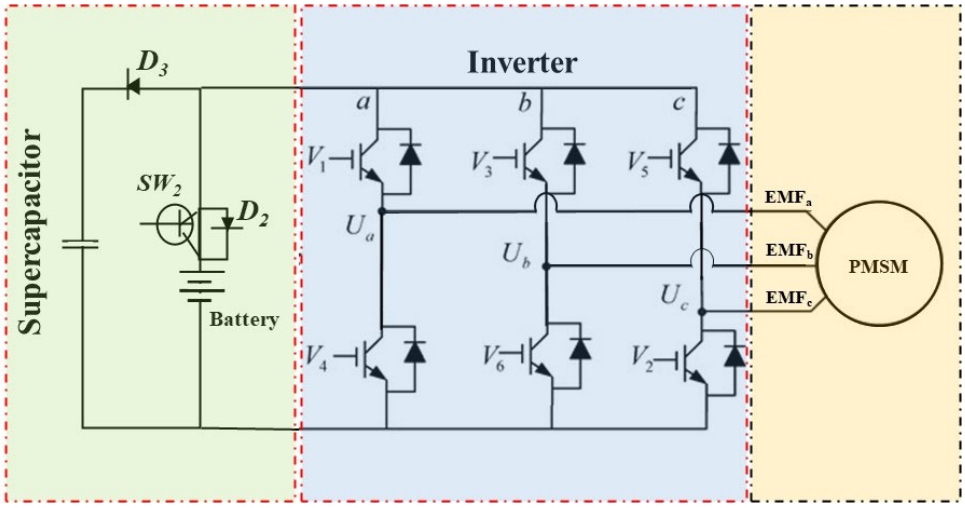

Figure 7. The corresponding circuits of the newly devised HESP, the three-phase inverter, and the PMSM.

During the braking scenario, six insulated gate bipolar transistors (IGBTs) are activated according to the rotor position sequence. This is determined through a Hall effect sensor. High-side half-bridge IGBT regenerative braking will not work, while the low-side switch is modulated through a proportional–integral (PI) controller. Figure 8 shows the back-EMF waveforms, armature current, and switching patterns in the regenerative braking scenario.

This study involved an examination of the dynamic adhesive energy requirements for the battery electric vehicle powertrain with a foundation in vehicle kinematics including rolling resistance force, aerodynamic drag force, grading force, and wheel force.

Rolling resistance occurs while the tire is rolling. The rolling resistance force F_R is expressed as

$$F_R\,(t) = K_r \cdot m \cdot g \tag{1}$$

where K_r is the rolling resistance (vehicle), typical values are 0.007–0.015, m is the mass of the vehicle (kg), and g is the gravitational constant which is 9.807 (m/s^2) [12].

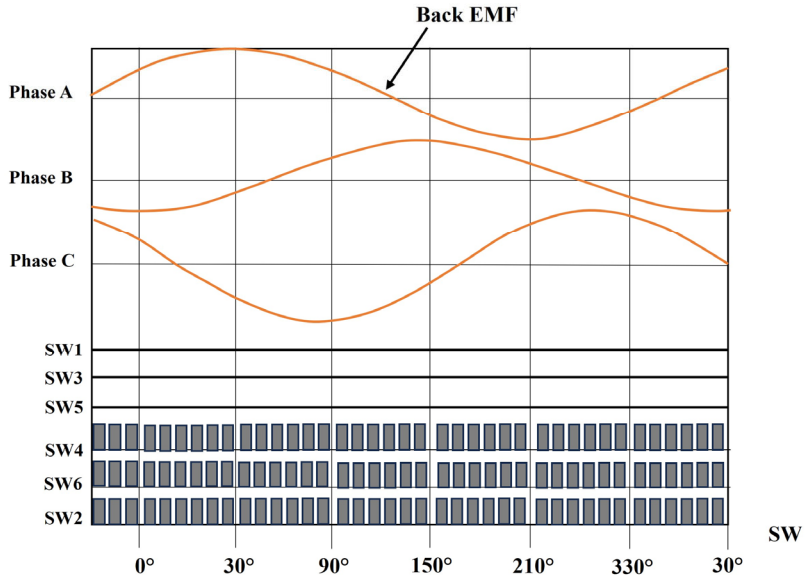

Figure 8. Back-EMF waveform of armature currents, and the switching template regenerative braking scenario.

Aerodynamic drag force inevitably comes into contact with aerodynamic drag (i.e., external flow and internal flow) during driving, and aerodynamic drag force (F_A) is expressed as [12]

$$F_A(t) = 0.5\rho_a C_a A_e(v_{vehicle} - v_{wind}) \quad (2)$$

where ρ_a is the density of air (kg/m^3) depending on humidity, temperature, pressure, and altitude at sea level, the temperature is 25 °C, and the standard atmospheric pressure is 1013.25 pascals, where ρ_a is 1225 (kg/m^3), C_a is the aerodynamic drag coefficient, the normal value is 0.25–0.35, A_e is the cross-sectional area of the vehicle (m^2), $v_{vehicle}$ is the vehicle speed (m/s), v_{wind} is the wind speed (m/s) [13].

The gradient force (F_G) acts parallel to the road due to the road inclination and is shown as

$$F_G(t) = mgsin\ (\alpha) \quad (3)$$

where α is the angle between the road level and the horizontal plane of the vehicle (radians).

$$\alpha = tan^{-1}\ (\frac{d_v}{d_h}) \quad (4)$$

d_v and d_h are the vertical distances and horizontal distances, respectively.

Wheel force F_W is the force exerted by the vehicle against the wheels to maintain speed and is expressed as

$$F_W\ (t) = F\ (t) + F_A\ (t) + F_R\ (t) + F_G\ (t) \quad (5)$$

If $F_W\ (t)$ is positive, it will accelerate the car and, if it is negative, it destroys the regenerated force or frictional braking. The maximum traction (F_{max}) on the wheel is controlled by the normal force on the wheel (F_N) or by the coefficient of friction (C_f) between the tire and the road, which is defined as

$$F_{max} = C_f \cdot F_N \quad (6)$$

The wheel power (P_w) can be determined by the product of traction force acting on the wheels (F_w) and vehicle speed ($v_{vehicle}$).

$$P_W\ (t) = F_W\ (t) \cdot v_{vehicle}\ (t) \quad (7)$$

The total energy available to the wheels can be determined by

$$E_W(t) = \int_o^t P_W(t)dt \tag{8}$$

The relationship between velocity and acceleration time is defined as follows:

$$V = at = \frac{dv}{dt}\, t \tag{9}$$

Acceleration work $W = FD$, acceleration force $F = ma$, where the distance (D) is in meters [13]

In Figure 9, the control arrangement for the RBS comprises both an ANN and a PI controller. Normally, during braking operations, the kinematic energy is progressively channeled to the SC and subsequently to the battery (i.e., HESP). However, the HESP rarely reaches its full capacity, making it impossible to add extra charges in exceptional cases. To counterbalance the surplus braking energy, the involvement of the rear-wheel mechanical brakes plays a vital role in distributing the braking force effectively [12–15]. In Table 2 the characteristics of the battery electric vehicle and the driving simulation are presented.

$$F_{car} = F_{front} + F_{rear} \tag{10}$$

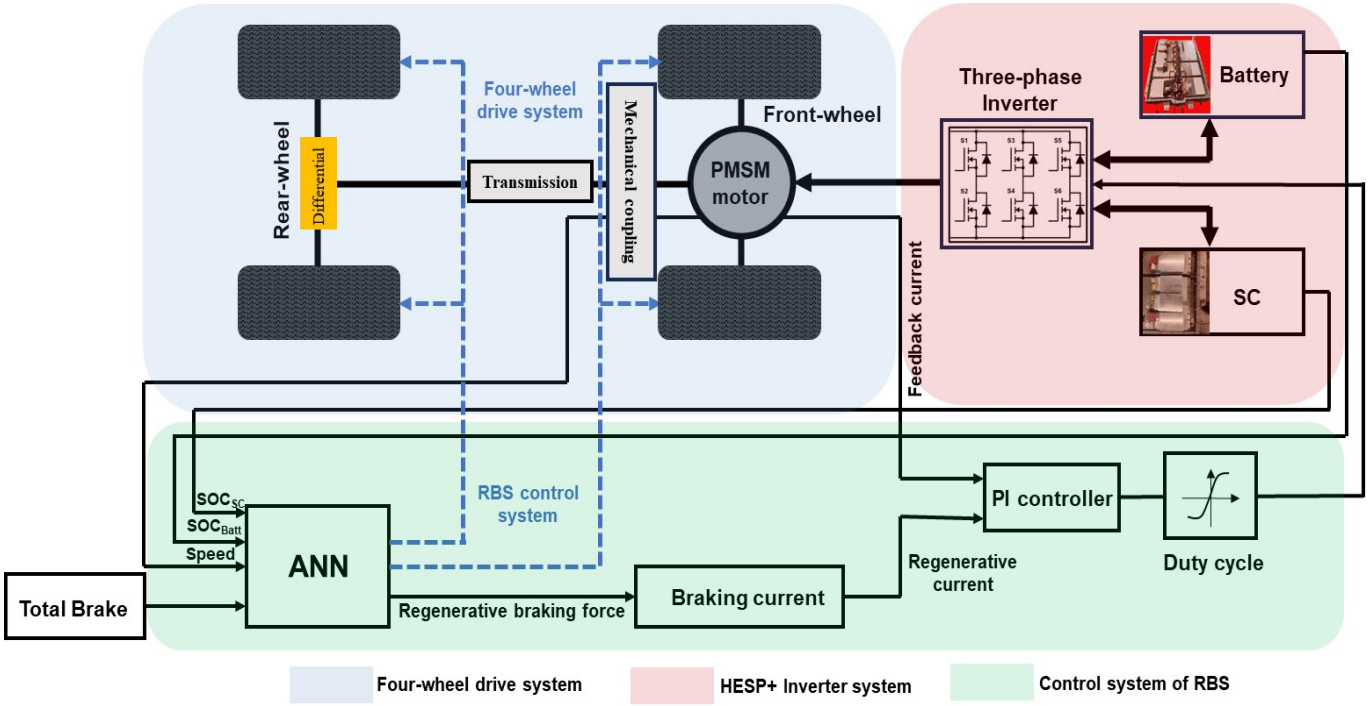

Figure 9. Structure of the regenerative braking system control.

Table 2. Characteristic parameters of the battery electric vehicle and driving.

Variable	Symbol	Value
Mass of the BEV	m	2210 kg
Gravitational constant	g	9.81 m/s^2
Air density	Pa	1.22 kg/m^3
Slope angle	θ	0 degrees
Aerodynamic drag coefficient	Ca	0.25–0.35 m
Rolling resistance coefficient	Kr	0.012

The use of an ANN to enhance the performance of an RBS is an innovative approach to novel architecture. An ANN resembles the structure and functioning of the human brain, and it can learn complex patterns and relationships from data. Using an ANN to increase the efficiency of regenerative braking is a form of optimizing the energy recovery process during braking in vehicles. Figure 10 shows that the RSB control mechanism incorporates an ANN-equipped three-layer multilayer perceptron (MLP) algorithmic scheme [16]. This control mechanism adjusts the braking force between the front and rear wheels. The inputs encompass the vehicle speed, the states of charge (SOCs) for both the SC and the battery, and the number of braking times per driving cycle. The consequences of the ANN algorithmic scheme comprise the mechanical braking forces exerted on the front and rear wheels, along with the regenerative braking force applied to the front wheel. MATLAB was used to simulate braking force (i.e., rear–front, regenerative braking force) on all 522 input combinations. However, selecting a three-layer MLP of the artificial neural network will enable it to receive more data capacity. Support for a total of 522 inputs means the model can withstand a wide range of operating conditions and environmental factors that can affect the performance of an RBS, which can be adapted to various real-world situations effectively. Figure 11 shows the simulated drivetrain configuration in MATLAB/SIMULINK R2016a. Meanwhile, the layer contained in the algorithmic framework contains 5 neurons with sigmoid activation functions as shown below.

$$f_{(u)} = \frac{1}{1 + e^{-u/t}} \tag{11}$$

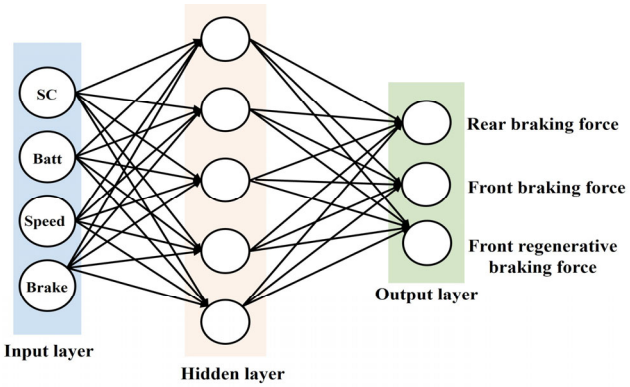

Figure 10. The algorithmic scheme of an artificial neural network.

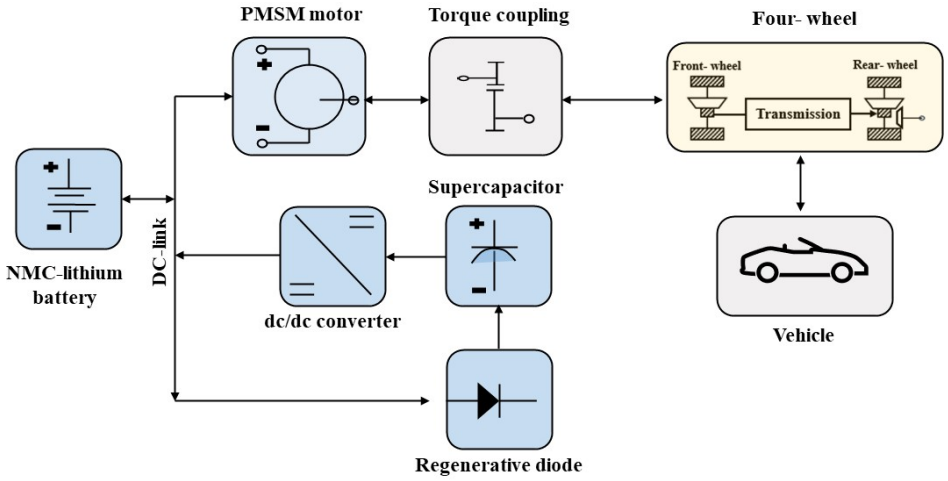

Figure 11. Simulated drivetrain configuration using MATLAB/SIMULINK.

The evaluation of the MLP algorithmic scheme equipped with the ANN involved the utilization of the NRMSE [17–22]. Table 3 delineates the drive cycle, a crucial factor ensuring the accuracy of simulation outcomes, particularly in braking scenarios.

$$NRMSE = \frac{\sum(S_i - O_i)^2}{\sum_{O_i} 2} \quad (12)$$

where S and O are the estimated and target results, respectively, and i is the data unit number. In this study, the NRMSE values were determined to be 0.015, 0.019, and 0.022 for the mechanical braking forces of the rear and front wheels, as well as regenerative braking force applied to the front wheel.

Table 3. Training drive cycle parameters.

Parameter	Value	Unit
Name of cycle	EUDC	-
Driving distance	6955.19	m
Time (total)	408.25	s
Percent of accelerating time	43.76	%
Percent of decelerating time	32.18	%
Percent of braking time	20.82	%
Percent of cruising time	19.06	%
Speed (average)	62.60	km/h
Maximum speed	79.22	km/h
Positive acceleration (average)	0.43	m/s^2
Negative acceleration (average)	−0.46	m/s^2

An ANN is a structure that generates braking force including rear, front, and force of regenerative braking, which causes the braking force on the front wheel to be converted into regenerated braking current (I) as follows [23–26]:

$$I = k \cdot F_{Regenerative\ breaking} \quad (13)$$

The PI controller modulates the regenerative braking current through the utilization of the PWM duty cycle algorithm scheme, allowing the regenerated braking force to enable safe driving (Figure 8).

To evaluate the overall performance of the RBS, the following equation was used:

$$\%\mu = \frac{\sum_{i=1}^{n} \Delta E_{Supercapacitor} + \sum_{i=1}^{n} E_{Battery}}{\sum_{i=1}^{n} \Delta E_{kinematic}} \times (100) \quad (14)$$

In Equation (14), n is the number of cars slowing or braking, $\Delta E_{Supercapacitor}$ is variation in the energy stored (SC module) before and after braking.

$$\Delta E_{Supercapacitor} = 0.5 \cdot C(V_2{}^2 - V_1{}^2) \quad (15)$$

where $\Delta E_{Battery}$ is the accumulated energy (battery) under braking (J), C is the module of supercapacitor capacity (Farad), V_1 and V_2 are the voltage of the SC module before and after braking, respectively.

$$\Delta E_{Battery} = \int_{t1}^{t2} (V_{Battery} i_{Battery} - R(t) i_{battery}^2) dt \quad (16)$$

where R is battery charge resistance, $V_{battery}$ is battery voltage, $i_{battery}$ is battery current, t_1 and t_2 are the starting and ending points of braking, and $\Delta E_{kinematic}$ is the kinematic energy (J) with variation of the vehicle, shown as

$$\Delta E_{Kinematic} = 0.5 \cdot m \cdot (v_2^2 - v_1^2) \quad (17)$$

where m is vehicle mass, v_1 is speed of the vehicle before braking, and v_2 is speed of the vehicle after braking [12].

4. Simulation and Experimental Results

In this study, simulations were conducted using MATLAB/SIMULINK for the proposed RBS program in the BMW X model. The simulations were performed for the EU legislative cycles (extra-urban drive cycle, EUDC) with a drive cycle distance of 6955.19 m and a total travel time of 408.25 s. The average speed per drive cycle was recorded as 62.6 km/h. Table 4 shows the experiment's statistical test before and after implementing an HESP-RBS in an EV. From the table data, it is found that the average driving distances and drive cycles of a traditional BEV are 245.46 km (~35 cycles), for an RBS-only battery they are 282.56 km (~40 cycles), and for the HESP-RBS they are 338.78 km (~48 cycles).

Table 4. The experimental driving distance and drive cycles of EV.

Statistical Test	Driving Distance (km)					Drive Cycles				
Traditional BEV	244.58	243.29	247.07	245.18	247.16	35.16	34.98	35.52	35.25	35.53
RBS-only battery	282.49	282.68	281.54	284.19	281.87	40.61	40.64	40.47	40.86	40.52
HESP-RBS	338.86	339.34	337.85	337.97	339.87	48.72	48.79	48.57	48.59	48.86

Table 5 presents the collated data for the simulated and experimental HESP consisting of an SC, NMC-lithium battery, three-phase PMSM, and on-board charger. In addition, to validate the model used in MATLAB/SIMULINK, a pilot program was made based on the performance of the speed test and speed reference with real vehicles (Figure 12). Table 6 shows the technical parameters of a three-phase permanent magnet synchronous motor, and Table 7 represents the technical parameters of the controller in the HESP.

Table 5. The simulated and experimental parameters of HESP.

Specifics	Simulation	Experimental
NMC-lithium battery	NMC-lithium-ion battery pack from ADVISOR 365 Volt 165 Ah 96 cells in series	NMC-lithium-ion battery pack 365 Volt 165 Ah 3 cells in series
Supercapacitor	SC module Maxwell Ultra Capacitor BoostCap 2.7 V 3000 Farad 140 cell in series total 380 V	SC module hybrid supercapacitor 2.7 V 3000 Farad 140 cell in series total 380 V
PMSM	Three-phase PMSM, 30/60 kW	Three-phase PMSM, 30/60 kW
On-Board charger	7 kW	7 kW
Measurement instrument	Power and data analysis YOKOGAWA DL350	

In Figure 13, the simulated speed profiles of the HESP-RBS in battery electric vehicles are illustrated for a single drive cycle. Within this cycle, the vehicle underwent acceleration, reaching an initial constant speed of approximately 60 km/h for a duration of 145 s, after which it decelerated and came to an idle state. The second cycle commenced 50 s after the start, during which the vehicle reached and maintained a consistent speed of approximately 75 km/h for a duration of 190 s before transitioning into the deceleration phase. Following a 50 s interval, the third and fourth cycles were approximately 100 km/h (230 s) and 115 km/h (295 s), respectively. The final cycle was initiated, during which the vehicle was propelled to a steady speed of 140 km/h and maintained for a period of 350 s. In addition, motor torque profiles that correspond to the cycles were made. The highest motor torque recorded was approximately 390 N.m. across all three scenarios. The black-shaded regions indicate

the regenerative braking energy that has been transferred and stored within the HESP. As the speed and the braking force of an EV increase, the kinetic energy of the vehicle will also increase. During braking the RBS captures the kinetic energy and converts it into electrical energy. Both increasing speed and braking force contribute to the improved performance of the RBS in an EV by providing more kinetic energy for regeneration. This observation underscores the efficacy of the suggested RBS control mechanism, as demonstrated in Figure 8. The experimental results of the motor properties in Figure 14 show the efficiency maps for all three motors in terms of torque–speed and planes with speed are highlighted in the torque velocity plane plot. In addition, Figure 15 also shows the behavior of the torque velocity characteristics of the PMSM within its complete operating range.

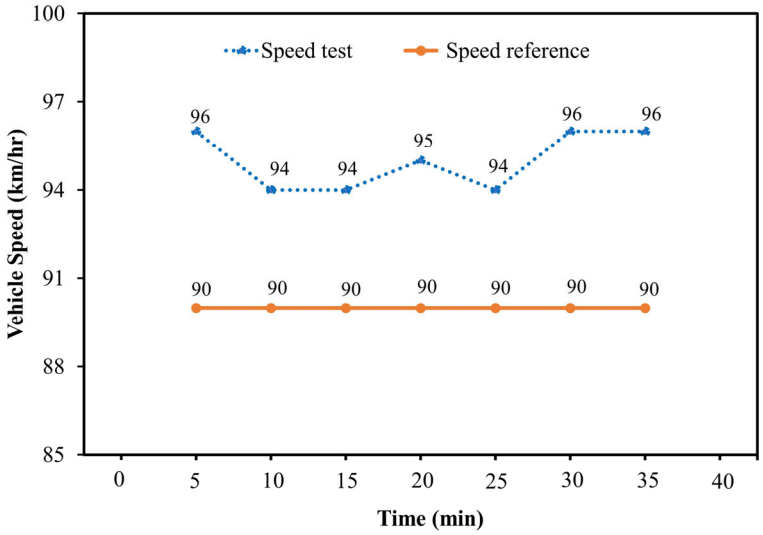

Figure 12. The simulations of the speed test and speed reference with a real vehicle were performed.

Table 6. Technical parameters of a three-phase PMSM.

Item	Specification	Value
PMSM	Rated Power (P_R)	30 kW
	Max. Power (P_M)	60 kW
	Battery Voltage (V_{batt})	365 v
	Net Weight (W_{net})	42 kg
	Rated Speed (S_R)	3340 rpm
	Max. Speed (S_M)	9000 rpm
	Rate Torque (T_R)	125 N·m
	Max. Torque (T_M)	390 N·m
	Max. Current (C_M)	320 A
	Protection Grade ($G_{Protect}$)	IP67
	Insulation Level (L_I)	H
	Cooling Method ($M_{cooling}$)	Water/Liquid Cooling

The mechanism of braking force between the front and rear wheels using the RBS-equipped ANN was studied. From the comparison, the largest proportion of the total braking force is applied to the front wheels (i.e., regenerative and mechanical forces). During the acceleration of the vehicle, the SC module provides additional power to the battery.

Table 7. Technical parameters of the controller.

Item	Specification	Value
Controller	Rated Voltage (R_{vol})	380 v
	Range of Working Voltage (R_{vol})	60–125%
	Output Rated Current ($R_{out,current}$)	168 A
	Output Max. Current ($M_{out,current}$)	330 A
	Grade of Protection ($G_{protect}$)	IP67
	Ambient Temperature (A_{temp})	−40~50 °C
	Mode of Control ($M_{control}$)	Vector Control
	Mode of Communication (M_{com})	CAN
	Net Weight (W_{net})	9.2 kg

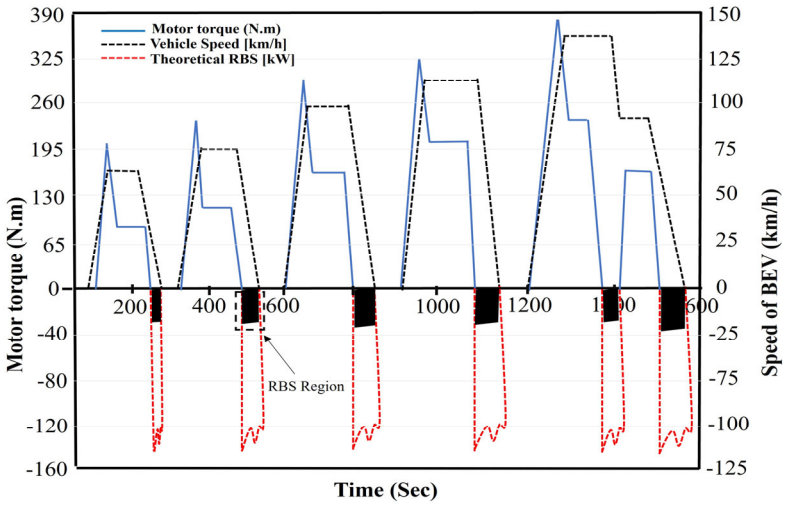

Figure 13. The simulated performance of motor torque and driving cycle with regenerative braking force.

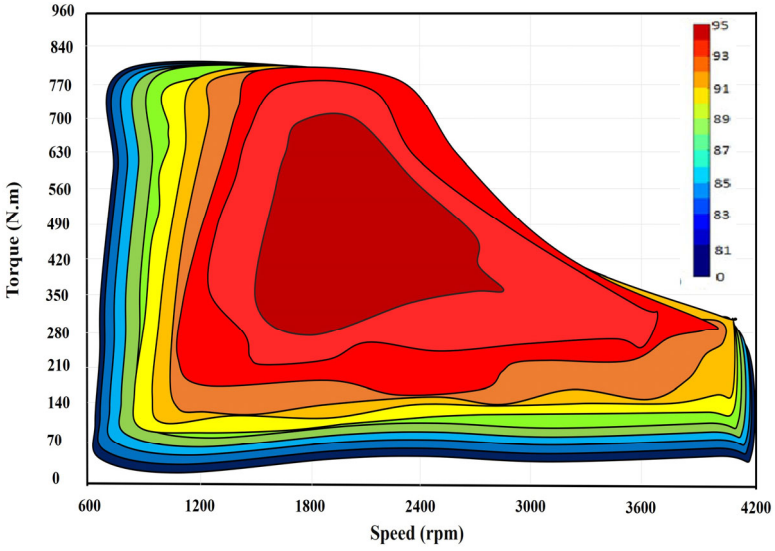

Figure 14. The efficiency map shapes and their associated loss contours of the PMSM.

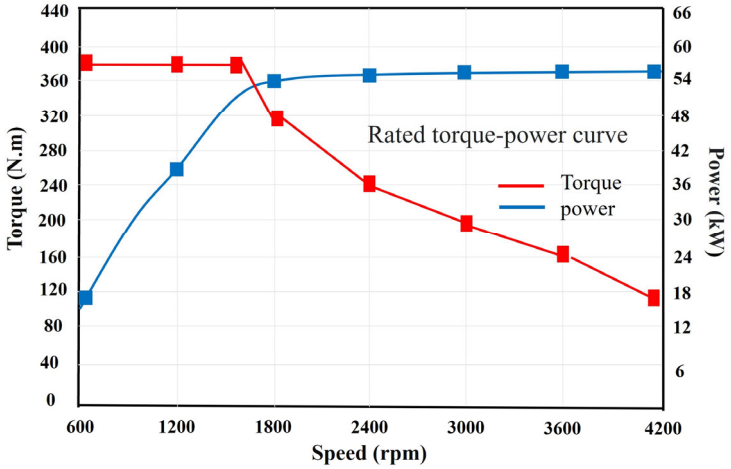

Figure 15. Rated torque and power curves for a typical engine.

Figure 16a,b illustrate the examination of the RBS control mechanism. The beginning state of charge (SOC) of the SC was set to be lower (89.8%) and higher (97.4%), with the highest safety at 97.6%, with corresponding battery SOCs of 82.7% and 83.4%, respectively. In Figure 16a, the beginning SOC is below the highest safety standard. The regenerated energy of braking is transferred to the SC and, after reaching the 97.6% standard, is transferred to the battery. In Figure 16b, the beginning SOC is above the highest safety standard, which allows regenerated braking energy to be transferred directly to storage in the battery. The energy transfer mechanism between the SC and battery in the HESP typically involves a control strategy aimed at optimizing the energy flow depending on factors such as energy demand, SOC of the components, and efficiency considerations. When the vehicle decelerates or brakes, kinetic energy is converted into electrical energy through regenerative braking. This energy is initially stored in the SC due to its high power density and ability to rapidly charge and discharge. Control algorithms monitor the SOC of both the SC and the battery. When the SC's SOC is above a certain threshold or when power demand exceeds the supercapacitor's capability, energy transfer occurs from the SC to the battery for long-term storage [10]. Figure 17 shows the driving distance of the electric vehicle from the simulation using the EUDC driving pattern in a traditional BEV, RBS-only battery, and HESP-RBS.

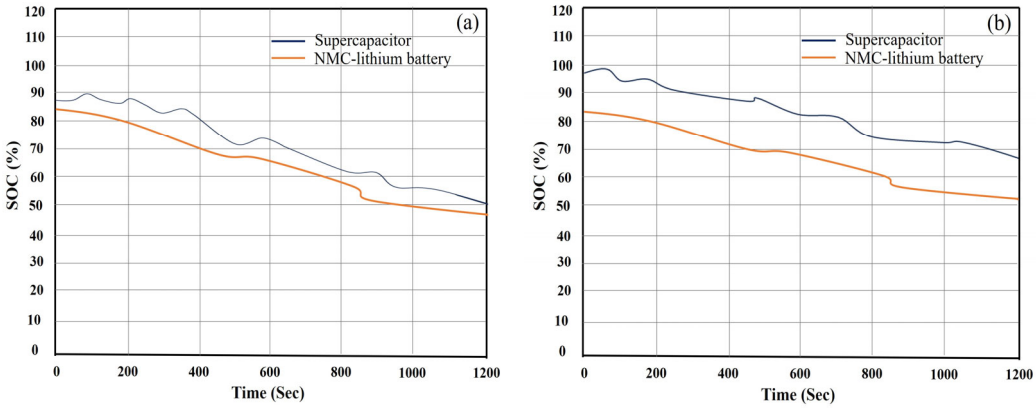

Figure 16. The state of charge (SOC) variation over time: (**a**) initial SOC: 89.8% (SC) and 84.6% (battery) and (**b**) initial SOC: 98.4% (SC) and 83.7% (battery).

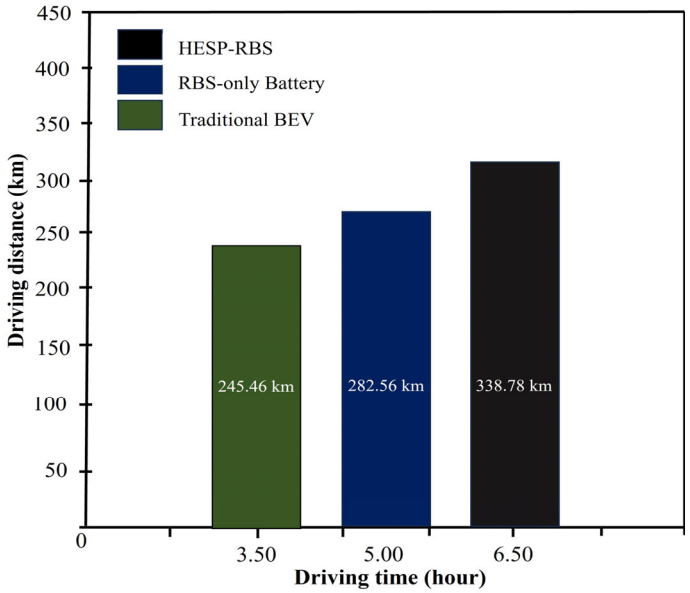

Figure 17. Driving distance of electric vehicles from simulation using the EUDC driving pattern.

Figure 18 illustrates the upcycling to a commercial-scale experimental arrangement of the RBS program, which includes the HESP, DC/DC chopper [27,28], and a three-phase PMSM. The specifications of these experimental components are provided in Table 5.



Figure 18. Experimental setup of the regenerative braking system.

The waveforms of the DC link voltage and current are shown in Figure 19 under a regenerative braking condition in which the battery and SC are activated. When the brake is applied, the RBS mechanism is activated to control the DC link voltage. The regenerated current is transferred to the SC, and when the SC voltage exceeds the maximum safety standard (97.6%), the mechanism transfers the regenerated current to the battery.

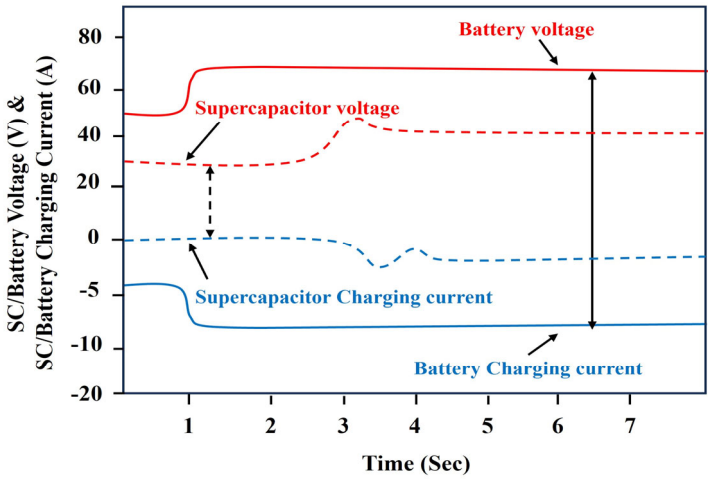

Figure 19. DC link voltage and current wave during regenerative braking scenario by SC and battery.

As shown in Figure 20a–c, the engagement of brakes led to a decrease in the back-EMFs, and the RBS control mechanism evenly allocated the braking force to the mechanical brakes of both the front and rear wheels.

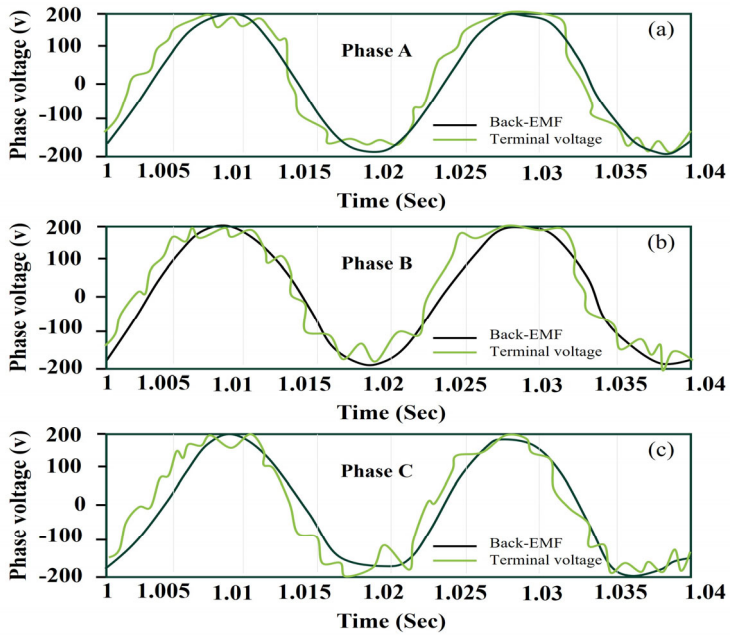

Figure 20. Back-EMF of the stator windings in normal operation and HESP activated regenerative braking scenario: (**a**) full diode bridge rectifier (**b**) active rectifier with sinusoid and (**c**) trapezoidal reference current.

In Figure 21, the DC link voltage across different operating periods is 1.25, 2.50, and 3.75, resulting in the corresponding motor speeds of 2500, 3000, and 3500 rpm, respectively.

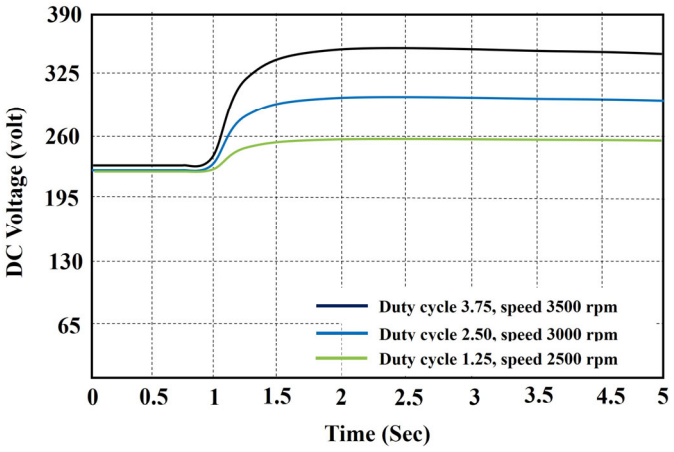

Figure 21. DC link voltage variation across different duty cycles.

The experimental outcomes provide validation for the effectiveness of the proposed ANN-equipped RBS program in significantly improving regenerative braking energy. This is supported by the observed increase in travel distance, with electric vehicles with HESP-RBS achieving a longer distance of 338.78 km (48 cycles) which is an increase of 93.32 km (13 cycles) compared to the traditional BEV distance of 245.46 km (35 cycles). The HESP, which uses hybrid energy storage sources from the SC and battery based on the RBS, can significantly improve the driving efficiency of electric vehicles. Table 8 compares the hybrid energy storage paradigm with the literature.

Table 8. Comparison of RBS-based energy storage systems for EV applications.

Source of HESP	Overall Cost	Control Complexity	Performance
Flywheel energy storage system [29]	High	High	- High power density - Fast response time - Long lifespan - Low maintenance
Battery/supercapacitor with BLDC motor [12]	Low	High	- The efficiency of the regenerative braking is increased - It needs a unidirectional DC/DC converter - Industrial scale (real car)
This work	Medium	High	- Low vehicle mass - Enhanced regenerative efficiency - Increased driving distance - Long lifespan

5. Conclusions

This study proposes the hybrid energy storage paradigm (HESP) for the regenerative braking system (RBS) of a battery electric vehicle (BEV) driven by a four-wheel PMSM. The ANN-equipped RBS mechanism is used to control the switching of the three-phase inverter and the force distribution of the BEV. Under the regenerative braking scenario, the ANN-equipped RBS program transfers the stored braking energy into the SC until the maximum safety standard (97.6%) is reached and then transfers the energy to the battery. In addition, the RBS is equipped with ANN with a three-layer MLP algorithm as a control mechanism. It helps the vehicle distribute braking force evenly between the front and rear wheels. Performance comparison of the HESP-RSB program is simulated under three scenarios: traditional BEV, RBS-only battery, and the HESP-RBS in an EUDC environment, given one drive cycle of 6955.19 m. From the test results, a traditional BEV can drive 245.46 km (35 cycles), the RBS-only battery can drive 282.56 km (40 cycles), and an electric vehicle with HESP-RBS can drive 338.78 km (48 cycles), which increases driving efficiency up to 93.32 km (13 cycles), or the regenerative efficiency increased by 38.01%

when compared with the traditional BEV. In addition, the HESP-RBS program increases vehicle acceleration and extends battery life for a long time.

Author Contributions: Conceptualization, P.T.; methodology, P.T. and W.K.; software, P.T.; validation, P.T. and W.K.; formal analysis, P.T. and W.K.; investigation, P.T.; resources, P.T. and W.K.; data curation, P.T. and W.K.; writing—original draft preparation, P.T. and W.K.; writing—review and editing, P.T. and W.K.; visualization, P.T. and W.K.; supervision, P.T.; project administration, P.T. and W.K.; funding acquisition, P.T. and W.K. All authors have read and agreed to the published version of the manuscript.

Funding: This research received no external funding.

Data Availability Statement: The original contributions presented in the study are included in the article, further inquiries can be directed to the corresponding authors.

Conflicts of Interest: The authors declare no conflict of interest.

References

1. Tao, A.; Liang, Q.; Kuai, P.; Ding, T. The Influence of Urban Sprawl on Air Pollution and the Mediating Effect of Vehicle Ownership. *Processes* **2021**, *9*, 1261. [CrossRef]
2. Badal, F.R.; Das, P.; Sarker, S.K.; Das, S.K. A Survey on Control Issues in Renewable Energy Integration and Microgrid. *Prot. Control. Mod. Power Syst.* **2019**, *4*, 8. [CrossRef]
3. Shafiq, S.; Irshad, U.; Al-Muhaini, M.; Djokic, S.; Akram, U. Reliability Evaluation of Composite Power Systems: Evaluating the Impact of Full and Plug-in Hybrid Electric Vehicles. *IEEE Access* **2020**, *8*, 114305–114314. [CrossRef]
4. Liu, J.; Liu, Z. In-cylinder thermochemical fuel reforming for high efficiency in ammonia spark-ignited engines through hydrogen generation from fuel-rich operations. *Int. J. Hydrogen Energy* **2024**, *54*, 837–848. [CrossRef]
5. Yang, R.; Liu, Z.; Liu, J. The methodology of decoupling fuel and thermal nitrogen oxides in multi-dimensional computational fluid dynamics combustion simulation of ammonia-hydrogen spark ignition engines. *Int. J. Hydrogen Energy* **2024**, *55*, 300–318. [CrossRef]
6. Yu, D.; Wang, W.; Zhang, H.; Xu, D. Research on Anti-Lock Braking Control Strategy of Distributed-Driven Electric Vehicle. *IEEE Access* **2020**, *8*, 162467–162478. [CrossRef]
7. Hu, X.; Xu, L.; Lin, X.; Pecht, M. Battery Lifetime Prognostics. *Joule* **2020**, *4*, 310–346. [CrossRef]
8. Enang, C.M.; Johnson, B.K. Bidirectional dc-dc Converter Control in Battery-Supercapacitor Hybrid Energy Storage System. In Proceedings of the 2020 IEEE Power & Energy Society Innovative Smart Grid Technologies Conference (ISGT), Washington, DC, USA, 17–20 February 2020; pp. 1–5.
9. Lien, J.; Mazalov, V.; Melnik, A.; Zheng, J. Wardrop Equilibrium for Networks with the BPR Latency Function. In *Discrete Optimization and Operations Research*; Springer: Cham, Switzerland, 2016; Volume 9869, pp. 37–49.
10. Kiddee, K.; Keyoonwong, W.; Khan-Ngern, W. An HSC/battery energy storage system-based regenerative braking system control mechanism for battery electric vehicles. *IEEJ Trans. Electr. Electron. Eng.* **2018**, *14*, 457–466. [CrossRef]
11. Zhang, C.; Min, H.; Yu, Y.; Wang, D.; Luke, J.; Opila, D.; Saxena, S. Using CPE Function to Size Capacitor Storage for Electric Vehicles and Quantifying Battery Degradation during Different Driving Cycles. *Energies* **2016**, *9*, 903. [CrossRef]
12. Naseri, F.; Farjah, E.; Ghanbari, T. An Efficient Regenerative Braking System Based on Battery/Supercapacitor for Electric, Hybrid, and Plug-In Hybrid Electric Vehicles with BLDC Motor. *IEEE Trans. Veh. Technol.* **2017**, *66*, 3724–3738. [CrossRef]
13. Reddy, K.S.; Veeranna, S.B. Design Parameters of Electric Vehicle. In Proceedings of the 2020 International Conference on Power Electronics & IoT Applications in Renewable Energy and its Control (PARC), Mathura, India, 28–29 February 2020; pp. 14–21.
14. Xu, Q.; Wang, F.; Zhang, X.; Cui, S. Research on the Efficiency Optimization Control of the Regenerative Braking System of Hybrid Electrical Vehicle Based on Electrical Variable Transmission. *IEEE Access* **2019**, *7*, 116823–116834. [CrossRef]
15. Kaleg, S.; Hapid, A.; Kurniasih, M. Electric Vehicle Conversion Based on Distance, Speed and Cost Requirements. *Energy Procedia* **2015**, *68*, 446–454. [CrossRef]
16. Xu, G.; Li, W.; Xu, K.; Song, Z. An Intelligent Regenerative Braking Strategy for Electric Vehicles. *Energies* **2011**, *4*, 1461–1477. [CrossRef]
17. Xu, P.; lu, W.; Wang, B. A semi-supervised learning framework for gas chimney detection based on sparse autoencoder and TSVM. *J. Geophys. Eng.* **2019**, *16*, 52–61. [CrossRef]
18. Amine, M.; Djoudi, K. Vehicles detection using the MLP and the correlation measurement. In Proceedings of the 2019 International Conference on Advanced Electrical Engineering (ICAEE), Algiers, Algeria, 19–21 November 2019; pp. 1–5.
19. Orrù, P.F.; Zoccheddu, A.; Sassu, L.; Mattia, C.; Cozza, R.; Arena, S. Machine Learning Approach Using MLP and SVM Algorithms for the Fault Prediction of a Centrifugal Pump in the Oil and Gas Industry. *Sustainability* **2020**, *12*, 4776. [CrossRef]
20. Hastie, T.; Tibshirani, R.; Friedman, J.; Franklin, J. The Elements of Statistical Learning: Data Mining, Inference, and Prediction. *Math. Intell.* **2004**, *27*, 83–85.

21. Sim, G.; Min, K.; Ahn, S.; Sunwoo, M.; Jo, K. Deceleration Planning Algorithm Based on Classified Multi-Layer Perceptron Models for Smart Regenerative Braking of EV in Diverse Deceleration Conditions. *Sensors* **2019**, *19*, 4020. [CrossRef] [PubMed]
22. Ouazzani Chahidi, L.; Fossa, M.; Priarone, A.; Mechaqrane, A. Evaluation of Supervised Learning Models in Predicting Greenhouse Energy Demand and Production for Intelligent and Sustainable Operations. *Energies* **2021**, *14*, 6297. [CrossRef]
23. Talaviya, T.; Shah, D.; Patel, N.; Yagnik, H.; Shah, M. Implementation of artificial intelligence in agriculture for optimisation of irrigation and application of pesticides and herbicides. *Artif. Intell. Agric.* **2020**, *4*, 58–73. [CrossRef]
24. Kommabathula Babu, P. ANN Equipped Controller for Anti-locking Braking System. *Int. J. Innov. Technol. Explor. Eng.* **2019**, *8*, 2278–3075.
25. Zhu, Y.; Wu, H.; Zhang, J. Regenerative Braking Control Strategy for Electric Vehicles Based on Optimization of Switched Reluctance Generator Drive System. *IEEE Access* **2020**, *8*, 76671–76682. [CrossRef]
26. Tang, X.; Yang, W.; Hu, X.; Zhang, D. A novel simplified model for torsional vibration analysis of a series-parallel hybrid electric vehicle. *Mech. Syst. Signal Process.* **2016**, *85*, 329–338. [CrossRef]
27. Ko, S.-T.; Park, S.-S.; Lee, J.-H. Regenerative Battery Charging Control Method for PMSM Drive without a DC/DC Converter. *Electronics* **2019**, *8*, 1126. [CrossRef]
28. Duraisamy, Y.; Gunasekaran, S. Design and modeling of improved controller using DC source fed permanent magnet synchronous motor drive with enhanced DC-DC converter by reducing vibrations for industrial applications. *J. Vibroengineering* **2019**, *21*, 228–249. [CrossRef]
29. Erhan, K.; Özdemir, E. Prototype production and comparative analysis of high-speed flywheel energy storage systems during regenerative braking in hybrid and electric vehicles. *J. Energy Storage* **2021**, *43*, 103237. [CrossRef]

Disclaimer/Publisher's Note: The statements, opinions and data contained in all publications are solely those of the individual author(s) and contributor(s) and not of MDPI and/or the editor(s). MDPI and/or the editor(s) disclaim responsibility for any injury to people or property resulting from any ideas, methods, instructions or products referred to in the content.